Cell shape independent FtsZ dynamics in synthetically remodeled cells

Short title: FtsZ dynamics in shapes

Bill Söderström[1*$], Alexander Badrutdinov[2],
Helena Chan[1], and Ulf Skoglund[1]

[1]Structural Cellular Biology Unit
[2] Mechanical Engineering and Microfabrication Support Section
Okinawa Institute of Science and Technology, 904-0495 Okinawa, Japan

* Address correspondence to:
Mail Bill.soederstroem@oist.jp or soderstrombill@gmail.com,
Tel: +81 080-6483-7515, Fax : +81 098-982-3420
$ Twitter: @BillSoderstrom

Key words: FtsZ, Micron pillars, STED, Z-square, Z-heart

Abstract

The FtsZ protein is a key regulator of bacterial cell division. It has been implicated in acting as a scaffolding protein for other division proteins, being a force generator during constriction, and more recently, as an active regulator of septal cell wall production. During an early stage of the division cycle, FtsZ assembles into a heterogeneous structure coined the “Z-ring” due to its resemblance to a ring confined by the midcell geometry. While *in vitro* experiments on supported lipid bilayers have shown that purified FtsZ can self-organize into a swirling ring roughly the diameter of a bacterial cell, it is not known how, and if, membrane curvature affects FtsZ assembly and dynamics *in vivo*.

To establish a framework for examining geometrical influences on proper Z-ring assembly and dynamics, we sculptured *Escherichia coli* cells into unnatural shapes, such as squares and hearts, using division- and cell wall-specific inhibitors in a micro fabrication scheme. This approach allowed us to examine FtsZ behavior in engineered “Z-squares” and “Z-hearts”, and in giant cells up to 50 times their normal volume. Quantification of super-resolution STimulated Emission Depletion (STED) nanoscopy data showed that FtsZ densities in sculptured cells maintained the same dimensions as their wild-type counterparts. Additionally, time-resolved fluorescence measurements revealed that FtsZ dynamics were generally conserved in a wide range of cell shapes. Based on our results, we conclude that the underlying membrane environment is not a deciding factor for FtsZ filament maintenance and treadmilling *in vivo*.

Introduction

Most bacterial cells divide by binary fission, whereby one mother cell splits into two identical daughters [1-3]. Decades of study have led to a detailed understanding of how the cell division machinery, the divisome, carries out this task during the later stages of the cell cycle [4,5]. At the heart of this process is the eukaryotic tubulin homologue, FtsZ [6] that, together with its membrane anchors ZipA and FtsA, forms an intermediate structure called the proto-ring (Fig. 1a) [7]. Functioning as a recruitment base, the proto-ring components then enlist the remaining essential division proteins to form a mature 'divisome' [5]. As soon as it is fully assembled, the divisome starts to constrict the cell envelope by reshaping the septal geometry, ultimately leading to sequential closure of the inner and outer membranes [8-10].

In rod-shaped model bacteria such as *Escherichia coli* and *Bacillus subtilis*, FtsZ is believed to organize into short bundles of filaments, roughly 100 nm in length [11,12], that treadmill at the septum with a circumferential velocity in the order of 20-30 nm/s [13-15]. The treadmilling filaments guide and regulate septal peptidoglycan (PG-) production and ingrowth, leading up to septation [16]. This mode of action may be limited to rod-shaped bacteria that have two separate PG-machineries, as opposed to cocci, which have only one PG-machinery that is capable of finalizing division in cells with inhibited FtsZ dynamics [17].

At a late stage of membrane constriction, but prior to inner membrane fusion, FtsZ disassembles from midcell, indicating the possible existence of an upper limit of ring curvature [6,9]. However, other geometrical constraints that might govern Z-ring maintenance and stability are currently unclear. We were curious as to whether geometrical changes to cell shape would influence Z-ring formation and dynamics. In

93 this study, we examined FtsZ formation, organization and behavior in *E. coli* cells that
94 were sculptured into complex geometrical shapes in micron sized holes.
95
96 **Results**
97 *FtsZ structure and dynamics in Z-rings are not sensitive to increased ring size*
98 As a reference for unmodified division rings, we imaged Z-rings in *E. coli* cells
99 expressing FtsZ-mNeonGreen as the only source of FtsZ [18]. Under our experimental
100 conditions, this strain produced normal-looking, sharp Z-rings (Supplementary Fig. S1)
101 and grew and divided similarly to wild-type (WT) *E. coli* (MC4100) (Supplementary Fig.
102 S2a-e). We then trapped the cells in a vertical position in micron-sized holes that were
103 produced in agarose pads using silica micron pillar arrays [14] (Fig. 1b, Supplementary
104 Fig. S3), and imaged the cells using super-resolution time-gated Stimulated Emission
105 Depletion (gSTED) nanoscopy. In these standing cells, a heterogeneous Z-ring with
106 distinct FtsZ-mNeonGreen densities was clearly seen traversing the circumference of
107 the cell (Fig. 1c), similar to what has been observed before [12,14].
108 Previous work has shown that FtsZ densities generally maintain the same length
109 throughout envelope constriction [12,14]. We wanted to see if this was also true for cells
110 growing in the opposite direction, *i.e.* would FtsZ densities maintain the same
111 dimensions in Z-rings of cells with increased diameter at midcell? In order to increase
112 cell diameter, we treated *E. coli* cells with A22 and cephalexin (hereafter collectively
113 referred to as 'drugs'), in a way similar to what has previously proven successful for
114 cell shape manipulations [19]. A22 disrupts MreB dynamics and therefore perturbs the
115 characteristic rod-shape of *E. coli* cells [20,21], while cephalexin blocks cell division by
116 inhibiting the transpeptidase activity of FtsI [22]. The net effect of this dual drug treatment

117 is the growth of cells into shapeable blebs that are unable to divide (Supplementary
118 Fig. S4a).
119 As long as cell width remains less than cell length, FtsZ molecules should be directed
120 to midcell by the Min system [19], such that a ring-like structure should be observed in
121 the xy-plane of vertically-oriented, standing cells (Fig. 1b). To confirm this, we exposed
122 *E. coli* cells expressing FtsZ-mNeonGreen to drugs, and then trapped the cells
123 vertically in holes with a depth of 4.5 - 6 μm, and a diameter of up to 3.5 μm. Depending
124 on the size of the holes, cells were incubated between 120 and 240 minutes prior to
125 imaging; over-incubation resulted in cells that outgrew the holes (Supplementary Fig.
126 S4b. Letting cells grow for long time (> 10 h) produced giant blobs with internalized
127 FtsZ-mNeonGreen chain, see SI Text). We found "normal-looking" Z-rings that
128 spanned the midcell circumference for the entire range of cell diameters that were
129 imaged (~ 1 - 3 μm) (Fig. 1d-e). Importantly, confocal Z-stacks showed that each cell
130 contained only one Z-ring (Supplementary Fig. S5 and Movie SM1). Close inspection
131 of STED images revealed that the Z-rings in larger cells were composed of fluorescent
132 densities (Fig. 1f) with average lengths and widths of 132 ± 48 nm and 88 ± 9 (n =
133 172), respectively, which were similar ($p > 0.05$) to Z-ring densities in untreated cells
134 (Fig. 1g).
135 After we had established that large Z-rings can form in cells with increased diameter,
136 we proceeded to calculate FtsZ dynamics in these larger rings. However, strains
137 expressing FtsZ-FP as the only source of FtsZ have been shown to have a phenotype
138 similar to that of FtsZ mutants deficient in GTPase activity, with severely impaired
139 treadmilling speed [13]. Therefore, we chose to image cells that expressed FtsZ-GFP
140 from an ectopic locus on the chromosome, in addition to native FtsZ [23]. Earlier studies
141 showed that FtsZ-GFP, when expressed at levels below 50 % of total cellular FtsZ

142 levels, caused no observable phenotypic changes [9,12,23,24]. In our experimental setup,
143 FtsZ-GFP was expressed at ~ 30 % of total FtsZ levels (Supplementary Fig. S2).
144 Structured Illumination Microscopy (SIM) of drug-treated *E. coli* cells expressing FtsZ-
145 GFP showed large heterogeneous rings that were similar to those of FtsZ-
146 mNeonGreen (Fig. 1h - k). Time-lapse images revealed that FtsZ densities moved
147 around the midcell circumference, even in Z-rings with a diameter up to three times
148 larger than that of a WT cell (Supplementary Movie SM2). There was no difference in
149 the speed of individual densities in the rings of untreated cells compared to those in
150 sculptured cells that had a diameter 50 - 200 % larger than WT (26 ± 15 nm/s and 30
151 ± 18 nm/s, respectively) (Fig. 1l - m), suggesting that filament treadmilling speed is not
152 influenced by the length of the cell circumference. ZipA-GFP, an FtsZ membrane
153 anchor, also moved at essentially the same speed in both normal- and large-sized
154 rings (26 ± 8 nm/s) (Supplementary Fig. S6 and Movie SM3), which is comparable to
155 previously reported speeds [14].
156 Since treadmilling behavior of FtsZ in large cells was very similar to that in WT cells,
157 we were curious to see whether FtsZ subunit exchange in the rings would also be
158 similar. To assess this, we performed Fluorescence Recovery After Photobleaching
159 (FRAP) experiments on both untreated and drug-treated cells. We bleached half of
160 the FtsZ-GFP molecules in the rings of standing cells and monitored fluorescence
161 recovery over time (Fig. 2a). Z-rings in untreated cells had a mean $t_{1/2}$ recovery time
162 of 8.4 ± 1.9 sec, n = 23 (Fig. 2b), consistent with previous studies [14,25]. Surprisingly,
163 the average $t_{1/2}$ recovery time was the same for Z-rings with a wide range of diameters
164 (Fig. 2b). We believe this reflects the formation of a greater number of FtsZ filaments
165 at the inner membrane of expanded cells, due to larger accessible surface area (Fig.
166 2c), while filament treadmilling speed remains unchanged.

167

168 *The 'FtsZ-square'*

169 Next, we wanted to know if drug-treated cells placed in deep (5 μm) rectangular
170 volumes would adapt to these shapes and effectively form 'Z-rectangles' or 'Z-
171 squares' instead of 'Z-rings'. Previous work has shown that cells can adapt to
172 rectangular shapes in shallow wells, approximately 1 μm deep [19]. Here, we produced
173 quadrilateral patterns in agarose pads using silica micron pillar arrays similar to those
174 previously described [14], with the exception that the pillars were rectangular and 5.5 ±
175 0.5 μm in height. Side lengths of the micron chambers were up to 3.5 μm in length
176 (Supplementary Fig. S7), resulting in well volumes up to 80 μm^3, roughly 50-fold larger
177 than the volume of a WT cell (assuming a WT cell size of 2 μm in length and 1 μm in
178 width) (Supplementary Fig. S8).

179 Drug-exposed cells expressing FtsZ-mNeonGreen were placed in rectangular micron
180 holes and incubated at room temperature for 300 - 420 minutes (longer incubation
181 times were needed due to increased well size). The cells adapted to their new shapes
182 and formed rectangular cuboids with only one "Z-square" per cell (Fig. 3a,
183 Supplementary Movie SM4). Notably, FtsZ densities were observed both in the sharp
184 corners and along the sides of the rectangles (Fig. 3b, Supplementary Fig. S9).
185 Quantification of the FtsZ-mNeonGreen densities showed that they had similar
186 dimensions to those in untreated cells, with an average length of 105.4 ± 39.6 nm and
187 width of 79.6 ± 18.2 nm (n = 147) (Fig. 3c). This suggests that FtsZ filament
188 dimensions *in vivo* are insensitive to membrane curvature (or lack thereof).

189 To generate a fluorescent FtsZ fusion protein that could be used for both super-
190 resolution STED imaging and examination of filament dynamics when grown in rich
191 media at 37 °C, we constructed a plasmid-expressed FtsZ-mCitrine fusion. FtsZ-

192 mCitrine was expressed from an IPTG-inducible, medium copy-number plasmid,
193 pTrc99a, at a level approximately equal to 30 % of total cellular FtsZ. Under these
194 conditions, FtsZ-mCitrine formed normal-looking, sharp Z-rings (Supplementary Figs.
195 S1 and S2). Cells expressing FtsZ-mCitrine were then exposed to drugs, trapped in
196 rectangular micron-sized holes, and incubated for 180 - 280 minutes at room
197 temperature before gSTED imaging. We found that FtsZ-mCitrine formed filaments
198 that were 118.3 ± 41.3 nm long and 86.3 ± 22.5 nm wide (n = 162), similar to FtsZ-
199 mNeonGreen filament dimensions (Fig. 3c, Supplementary Fig. S10), indicating that
200 fluorophore choice did not influence cluster dimensions in the rings. For consistency,
201 we also imaged rectangular cells expressing FtsZ-GFP from the chromosome using
202 SIM (Supplementary Fig. S10). All three strains tested adapted to the rectangular
203 shape, producing sharped-cornered "Z-rectangles".
204
205 *FtsZ dynamics in rectangular-shaped cells*
206 In order to examine the dynamics of FtsZ in rectangular cells, we performed time-lapse
207 imaging on cells expressing either FtsZ-mCitrine or FtsZ-GFP. Although a few
208 fluorescence spots were abnormally bright and immobile (~ 1 spot / 5 cells, with a
209 maximum of 2 spots in one cell) (Fig. 4b, Supplementary Movie SM7. Red arrow), the
210 majority of FtsZ densities were highly dynamic (Fig. 4a-b, Supplementary Movies SM5
211 - SM6). Note that the bright, immobile spots were excluded from treadmilling analyses.
212 Close inspection of time-lapse sequences suggested that FtsZ bundles in rectangular-
213 shaped cells may be able to treadmill, even in right-angled corners (Fig. 4b-c,
214 Supplementary Movie SM8). The average speed of FtsZ-mCitrine densities in
215 rectangular cells with perimeter lengths up to 13 μm (more than four times the
216 circumference of a WT cell) was 27.6 ± 12.5 nm/s (n = 109), which was consistent with

217 the measured treadmilling speed of FtsZ-GFP in rectangular cells (25.3 ± 11.3 nm/s,
218 n = 122) (Fig. 4d), large cylindrical cells (30 ± 18 nm/s, Fig. 1m) and untreated cells (~
219 25 nm/s) [13,14].
220 To determine whether the dynamics of FtsZ subunit exchange are affected by changes
221 to circumferential length and shape, we collected FRAP measurements on FtsZ
222 bundles in rectangular-shaped cells (Fig. 4e, Supplementary Movie SM9). The
223 recovery times of half-bleached rectangles of varying sizes matched those of rings,
224 with mean $t_{1/2}$ recovery times of 9.85 ± 2.58 s (n = 24) and 9.15 ± 2.55 s (n = 22) for
225 FtsZ-mCitrine and FtsZ-GFP, respectively (Fig. 4f). This suggests that subunit
226 exchange from the cytoplasmic FtsZ pool is independent of circumference length and
227 membrane curvature. The data thus far indicate that the maintenance and dynamics
228 of FtsZ filaments are preserved in both large Z-rings and Z-rectangles of varying size.
229
230 *FtsZ dimensions and dynamics in heart-shaped cells*
231 To examine whether FtsZ could literally be (at) the heart of cell division, we engineered
232 micron pillar arrays that were heart-shaped (Supplementary Fig. S11). Heart shapes
233 were chosen because they would sculpt cells in such a way that highly curved, straight,
234 and angled membrane segments would be present within a single cell. Drug-treated
235 *E. coli* cells expressing cytoplasmic GFP, FtsZ-mNeonGreen or FtsZ-mCitrine were
236 sculptured into hearts as described above (Fig. 5a). Perhaps not surprisingly,
237 quantification of 155 individual FtsZ densities from the heart-shaped cells revealed
238 dimensions similar to those in round and rectangular cells (129 ± 44 nm long and 84
239 ± 9 nm wide) (Fig. 5b). We also found that the average speed of FtsZ-mCitrine in heart-
240 shaped cells (22 ± 10 nm/s, n = 44) was essentially the same as that in untreated cells
241 (Figure 5c, Supplementary Movie SM10).

242 For about one-third of the heart-shaped cells, we noticed bright spots of internalized
243 FtsZ-FP signal that accumulated close to the cell center (Figure 5c, green arrowhead).
244 Although we couldn't distinguish whether these were true FtsZ clusters or aggregated
245 protein, cytoplasmic clustering of FtsZ in WT cells have previously been reported [12].
246 Furthermore, although most hearts had FtsZ-FP signal spanning the full perimeter of
247 the cell, approximately 20 % were only "half full" (Fig. 5d, left). We do not fully
248 understand the underlying reason for this, however it is unlikely due to image focus or
249 cell tilt issues, as every cell was scanned in the z direction prior to imaging.
250 Nevertheless, when we subjected the heart-shaped cells to FRAP, fluorescence
251 recovery rates were equal for both full and half-full hearts (Fig. 5d), with mean $t_{1/2}$
252 recovery times of 7.1 ± 1.1 s (n = 24) and 6.9 ± 0.9 s (n = 9), respectively (Fig. 5e).
253
254 *FtsZ-"rings" form in complex cell shapes*
255 To explore if cell geometry plays a role in Z-"ring" formation, we set out to remodel
256 cells into other complex shapes. Even though highly complex-shaped bacteria occur
257 in nature, such as star-shaped bacteria [26], we wanted to test whether rod-shaped *E.*
258 *coli* cells would allow themselves to be drastically remodeled. Using micron pillars of
259 various shapes, we produced holes in agarose pads such that drug-exposed cells
260 could be sculptured into complex shapes, such as pentagons, half-moons, stars,
261 triangles and crosses (Fig. 6a, middle row. Supplementary Fig. S11). The cells
262 conformed remarkably well to these shapes, forming sharp boundary angles < 70°
263 (Fig. 6a, Star). After we confirmed that cells could adapt to these complex shapes, we
264 placed cells expressing FtsZ-mCitrine into the micron holes, allowed for reshaping to
265 occur, and then imaged the cells using STED nanoscopy. Cells of all tested shapes
266 produced easily recognizable FtsZ-"shapes" at midcell (Fig. 6a, bottom row).

267 Subsequent analysis of the lengths and widths of the FtsZ densities revealed little
268 difference in dimensions between the different shapes, suggesting a minimal role of
269 cell shape in determining FtsZ cluster dimensions *in vivo* (Fig. 6b). Additionally, time-
270 lapse imaging of cells expressing FtsZ-mCitrine in various shapes showed similar
271 dynamics to those measured in untreated cells (Supplementary Movie SM10).
272

273 **Conclusions**

274 Cells, both bacterial and eukaryotic, have the ability to adapt remarkably well to their
275 local environments [27-31], reverting to their original shapes after stress [32,33] and dividing
276 with striking midcell accuracy even when remodeled into irregular cell shapes [27,30]. In
277 bacteria, the tubulin homologue FtsZ assembles into a ring-like structure at midcell
278 and is responsible for overall maintenance of the cell division machinery [5,6]. The
279 general dynamics and organization of the FtsZ-ring have been shown to be quite
280 similar across many bacterial species [11,13-15,17,34-37]. Common to these species is
281 confinement of the FtsZ-ring to a circular geometry at midcell. Strikingly, when purified
282 FtsZ (together with its membrane anchor FtsA) is placed on supported lipid bilayers, it
283 assembles into a dynamic, swirling ring-like assembly with a diameter resembling that
284 of wild-type *E. coli* cells (approximately 1 μm), hinting at an intrinsically preferred FtsZ-
285 ring curvature [6,38].
286 In this study, we characterized FtsZ midcell accumulation and dynamics in cell shape-
287 determining environments by 'looking through the Z-ring' along the long-axis of cells.
288 We observed normal-looking FtsZ-rings in cells with diameters three times the size
289 found in WT cells. However, this might not be surprising, considering only ~ 30 % of
290 the pool of FtsZ molecules are in the ring of WT cells at any given point in time [39].
291 Quantification of FtsZ dimensions revealed little variation between different cell

292 shapes, such as squares, pentagons, triangles and stars (on average 123 x 80 nm,
293 length x width, respectively, and summarized in Table 1), suggesting that local
294 membrane geometry has minimal influence on FtsZ cluster dimensions. Compared to
295 untreated cells, rectangular and heart-shaped cells with perimeter lengths more than
296 four times that of a WT cell exhibited similar overall dynamics of FtsZ, as FtsZ-FP
297 fluorescence densities treadmilled at the same average velocity and FtsZ subunit
298 exchange occurred at similar rates (Table 2), independent of cell shape and size.
299
300 In summary, our results from different shaped cells show that Z-"ring" formation and
301 dynamics are not limited to cells of a certain shape or size. This agrees with previous
302 findings, which show that internal cellular structures are maintained in cells that have
303 been reshaped into unnatural forms [19]. Our observation that FtsZ clusters conform to
304 the geometric shape of the membrane at midcell suggests that FtsZ-ring formation is
305 not affected by changes in membrane curvature. Indeed, cell shape and size are
306 important for proper cellular functions [40], however, with the many naturally-occurring
307 shape variations of bacteria [26,41], it is perhaps not surprising that FtsZ can adapt to
308 changing environments without compromising its own ability to maintain fundamental
309 functionality. Although our data do not explicitly show that sculptured cells can divide
310 (since downstream division proteins were inhibited), the fact that the dynamic
311 properties of FtsZ are conserved suggests that this may be possible. One particular
312 implication of this is the notion that the Z-ring can be decoupled from the division
313 process but with maintained dynamics, making treadmilling a possible requirement for
314 divisome assembly and organization in rod shaped model bacteria, as previously
315 suggested for cocci [17]. Presently, we have shown *in vivo* that *E. coli* FtsZ-ring
316 formation and dynamics are conserved, irrespective of cell shape and size.

317 **Methods**

318 *Bacterial growth*

319 Pre-cultures were grown overnight in 20 ml of rich media (LB) at 37 °C or M9 minimal
320 media supplemented with 1μg ml^{-1} thiamine, 0.2 % (w/v) glucose and 0.1 % (w/v)
321 casamino acids. The following morning, cultures were back-diluted 1:50 in either LB
322 or M9 (with supplements) and antibiotics (ampicillin 25 μg ml^{-1}) when needed, and
323 incubated at 30 °C or 37 °C.

324

325 *Fluorescent protein production*

326 Chromosomally-encoded FtsZ-mNeonGreen was integrated at the native *ftsZ* locus
327 and did not require any inducer [18]. Chromosomally-encoded FtsZ-GFP (strain BS001),
328 GFP^{CYTO} (strain BS008) and ZipA-GFP were induced with 2.5 μM, 5 μM and 50 μM
329 IPTG, respectively [9].

330 The plasmid pHC054 (*ftsZ-mCitrine*) was constructed using Gibson assembly [42] to
331 generate an IPTG-inducible FtsZ-mCitrine fusion expressed from pTrc99a [43]. PCR
332 was performed using Q5 High-Fidelity DNA polymerase (New England Biolabs). A
333 DNA fragment containing *ftsZ* was amplified from *E. coli* MC4100 genomic DNA using
334 primers FtsZ(F) (5'-caatttcacacaggaaacagaccatggatgtttgaaccaatggaac-3') and
335 FtsZ(R) (5'-gcccttgctcaccatctgcaggttgttgttatcagcttgcttacgcagg-3'). *mCitrine* was
336 amplified from mCitrine-N1 plasmid DNA using primers mCitrine(F) (5'-
337 cgtaagcaagctgataacaacaacctgcagatggtgagcaagggcgaggag-3') and mCitrine(R) (5'-
338 ccgccaaaacagccaagcttttacttgtacagctcgtccatgc-3). pTrc99a plasmid DNA was
339 amplified using primers pTrc99a(F) (5'-ccatggtctgtttcctgtgtg-3') and pTrc99a(R) (5'-
340 aagcttggctgttttggcgg-3'). The *ftsZ* and *mCitrine* coding regions are separated by a
341 short linker encoding NNNLQ. The plasmid sequence was verified by DNA sequencing

342 (Fasmac, Japan). FtsZ-mCitrine expression was induced with 2.5 μM IPTG. All FtsZ
343 levels were quantified using Western blotting.
344
345 *Western blot analysis*
346 Cell extracts from a volume corresponding to 0.1 OD_{600} units were collected for each
347 strain to be analyzed. The extracts were suspended in loading buffer and resolved by
348 SDS-PAGE gel electrophoresis. Proteins were transferred to nitrocellulose
349 membranes using a semi-dry Transfer-Blot apparatus (Bio-Rad). The membranes
350 were blocked in 5 %(w/v) milk and probed with antisera to FtsZ (Agrisera, Sweden)
351 and detected using standard methods.
352
353 *Nanofabrication of micro arrays*
354 Micron pillars were engineered using two different, but related, approaches. The first
355 approach was used for round and square/rectangular micron pillars, and was adapted
356 from [14,15]. Briefly, using a multi-step process similar to that described in [44], micron-
357 scale pillars were fabricated on a silicon (Si) substrate by reactive ion etching. A
358 pattern of hard-baked photoresist was created on a Si surface using UV lithography,
359 to work as a mask for etching. Subsequent etching was performed using an Oxford
360 Plasmalab100 ICP180 CVD/Etch system, with a mixture of SF_6 and O_2 plasma as an
361 etchant. For our process, a SF_6:O_2 ratio of 1:1 was optimal. After etching, the
362 remaining photoresist was removed by O_2 plasma treatment. Pillar arrays (1 x 1 cm or
363 2 x 2 cm) with round pillars were engineered to contain one micron-sized pillar every
364 5 μm, with dimensions between 0.9 and 3.5 μm wide and 5.25 ± 0.75 μm high
365 (Supplementary Fig. S3). Pillar arrays (1 x 1 cm) with square pillars contained micron-

366 sized pillars approximately every 5 μm, with side lengths varying between 1.8 and 3.5
367 μm, and heights of 5.5 ± 0.5 μm (Supplementary Fig. S7).
368 To create more complex shapes, a second approach, based on electron beam
369 lithography was used. For this, the micron-scale structures were fabricated on a Si
370 substrate by a multi-step process, which was a combination of electron beam
371 lithography and reactive ion etching techniques. Similar approaches to silicon
372 patterning are described in a number of earlier works [44-47]. First, a pattern of e-beam
373 resist was created on a Si surface using e-beam lithography. A 50 nm-thick Ti layer
374 was then deposited, and a lift-off process was used to create a metal mask for etching.
375 The use of a metal mask, instead of a baked e-beam resist mask, was necessary due
376 to the high selectivity ratio required for generating structures only a few microns in
377 height. Finally, the etching process was performed as described above, using an
378 Oxford Plasmalab100 ICP180 CVD/Etch system and a mixture of SF_6 and O_2 plasma
379 as an etchant. For our process, a SF6:O_2 flow ratio of 3:2 produced the best results,
380 with a Si:Ti etching selectivity ratio of approximately 100:1. Increased concentration of
381 O_2 in the mixture has two effects: (i) it improves etching anisotropy, which is essential
382 for avoiding shape distortion from the undercut effect, and (ii) it reduces the selectivity
383 ratio, as the Si etch rate gets slower. After etching, the structures were characterized
384 using a Dektak surface profiler and SEM imaging. The micron structure arrays, which
385 contained various shapes (hearts, triangles, pentagons, half-moons and crosses),
386 were fabricated on 1 x 1 cm Si chips with inter-structure distances of approximately 5
387 μm, and structure heights of 5.5 ± 0.5 μm (Supplementary Fig. S11).
388
389
390

391 *Micron-sized chamber production and cell growth*

392 Liquefied agarose (5% w/v) in M9 minimal media (supplemented with 0.2 % glucose,
393 0.1 % casamino acids, 2 µg ml^{-1} thiamine, 40 µM A22 and 20 µg ml^{-1} cephalexin) was
394 dispersed on glass slides and the silica mold (pillar facing downwards) was placed on
395 top. The molds contained either round or rectangular pillars, or various geometrical
396 shapes, as described above. Once the agarose solidified, the mold was removed and
397 ~ 5 µl of live cell culture at OD_{600} 0.4 - 0.55 (pre-treated with 16 µM A22 for 10 - 15
398 minutes) was applied on top. To allow the cells to adapt to the different shapes, slides
399 were incubated at RT or 30 °C in a parafilm-sealed petri dish together with a wet tissue
400 to prevent drying. After incubation, cells were covered with a pre-cleaned cover glass
401 (♯1.5) for live cell imaging. For STED imaging, cells were first fixed with ice-cold
402 methanol for 5 minutes and carefully rinsed with PBS prior to cover glass application.
403

404 *Microscopy*

405 Gated STED (gSTED) images were acquired on a Leica TCS SP8 STED 3X system,
406 using a HC PL Apo 100x oil immersion objective with NA 1.40. Fluorophores were
407 excited using a white excitation laser operated at 488 nm for mNeonGreen and 509
408 nm for mCitrine. A STED depletion laser line was operated at 592 nm, using a
409 detection time-delay of 0.8 – 1.6 ns for both fluorophores. The total depletion laser
410 intensity was in the order of 20 - 40 MW/cm^2 for all STED imaging. The final pixel size
411 was 13 nm and scanning speed was either 400 or 600 Hz. The pinhole size was set
412 to 0.9 AU.

413 Epi-fluorescence and confocal images were acquired on either a Zeiss LSM780 or
414 Zeiss ELYRA PS1 (both equipped with a 100X 1.46NA plan Apo oil immersion
415 objective) with acquisition times between 0.3 and 2 sec. Time-lapse series for

416 generating kymographs were recorded at 2 sec intervals for a time period of at least
417 118 sec.
418 SIM images were acquired using a Zeiss ELYRA PS1 equipped with a pco.edge
419 sCMOS camera. The final pixel size in SIM images was 24 nm. Individual images were
420 acquired using an acquisition time of 200 ms per image (a total of 15 images were
421 acquired per SIM image reconstruction) and subsequently reconstructed from the raw
422 data using ZEN2012 software. SIM time-lapse movies (containing at least 14 frames)
423 were recorded without time delays between image stacks.
424 Confocal Z-stacks (focal plane ± ~ 3.5 µm) were acquired on a Leica TCS SP8 STED
425 3X system (operated in confocal mode) using predetermined optimal system settings
426 (Leica, LAS X), with 0.22 µm steps (resulting in 30-32 images per stack), and pinhole
427 size 1 AU. All imaging was performed at RT (~ 23-24 °C).
428
429 *FRAP measurements*
430 Confocal FRAP measurements were performed on a Zeiss LSM780 system using a
431 100x 1.4 NA plan Apo oil immersion objective and pinhole size 60 µm, as described
432 [14]. Bleaching was performed for 0.5-0.7 s using 100% laser power applied over the
433 region of interest. Data were collected in time intervals of 1 - 2 sec until steady state
434 was reached. Following background correction, and to account for overall successive
435 bleaching, the fluorescence intensity (F) of the bleached region (half a ring) was
436 normalized to the average ring fluorescence of an unbleached area of the same size,
437 for each time point (t); $F_{NORM}(t) = F_{BLEACHED}(t)/(F_{BLEACHED}(t) + {}_{UNBLEACHED}(t))$. All data
438 were exported to Origin9 Pro and data points were fitted to the single exponential
439 function $F(t) = F_{end} – (F_{end} – F_{start})^* e^{-kt}$, where F(t) is the fluorescence intensity at time
440 t, F_{end} is the fluorescence intensity at maximum recovery, F_{start} is the fluorescence

441 recovery momentarily after bleaching (at t = 0), and k is a free parameter. The recovery
442 half-time was then extracted from $t_{1/2}$ = ln 2 / k. Importantly, all cells were scanned
443 from top to bottom in order to find the division plane (in which the rings reside).
444
445 *Image analysis*
446 Image analysis was performed using Fiji. When necessary, images were background-
447 corrected using a rolling ball with radius 36. Image stacks were motion-corrected using
448 the plug-in StackReg. Kymographs were generated from time-lapse images using the
449 KymoResliceWide plugin (line width 5), from which treadmilling speeds were
450 calculated using the slope of the fluorescence trace, as previously described [38].
451 STED images were deconvolved using Huygens Professional deconvolution software
452 (SVI, the Netherlands). FtsZ-ring diameters were extracted from the average values
453 of the Gaussian fitted fluorescence profiles drawn from 12 - 6 o'clock and 3 - 9 o'clock.
454 Side lengths of shaped cells were determined by applying line profiles in ImageJ. The
455 lengths and widths of individual FtsZ densities were obtained using line scans (line
456 size 4) over at least 5 randomly selected individual fluorescence spots from each
457 deconvolved cell image, whereby a Gaussian was fitted to the intensity profiles in order
458 to extract the Full Width at Half Maximum (FWHM). Note that the long and short axes
459 of each individual FtsZ density were assigned as "length" and "width", respectively,
460 regardless of orientation relative to the membrane. FtsZ cluster dimensions are given
461 in mean ± S.D. n indicates number of cells, unless explicitly specified.
462
463 *Statistical analysis*
464 Boxes represent S.D., with red lines indicating mean. Whiskers on the box plots
465 encompass 95.5% of the distribution. For statistical analyses, two-tailed Student's *t*-

466 tests were performed using Origin Pro 9. A *p*-value of < 0.05 was considered as
467 statistically significant.
468
469 *Data availability*
470 Data presented and material used in this paper can be available upon request from
471 the authors.
472
473 **Acknowledgements**
474 The authors would like to thank Harold Erickson (Duke Uni.) for sharing the FtsZ-
475 mNeonGreen strain. Daniel Daley (Stockholm Uni.) is acknowledged for valuable
476 suggestions to improve the manuscript. BS is supported by JSPS KAKENH (grant
477 number JP17K15694). Work in the SCB unit at OIST is funded by core subsidy from
478 Okinawa Institute of Science and Technology Graduate University.
479
480 **Author contributions**
481 B.S. conceived the study and performed the experiments. A.B. and B.S. designed and
482 engineered the micron pillar arrays. H.C. contributed reagents. B.S. and U.S. analyzed
483 the data. B.S. wrote the manuscript with input from all authors.
484
485 **Competing financial interests**
486 The authors declare no conflicting or competing financial interests.
487

488

489 **References**

490 1 de Boer, P. A. Advances in understanding *E. coli* cell fission. *Curr Opin*
491 *Microbiol* **13**, 730-737, doi:10.1016/j.mib.2010.09.015 (2010).

492 2 Lutkenhaus, J., Pichoff, S. & Du, S. Bacterial cytokinesis: From Z ring to
493 divisome. *Cytoskeleton* **69**, 778-790, doi:10.1002/cm.21054 (2012).

494 3 Meier, E. L. & Goley, E. D. Form and function of the bacterial cytokinetic ring.
495 *Current opinion in cell biology* **26**, 19-27, doi:10.1016/j.ceb.2013.08.006
496 (2014).

497 4 Haeusser, D. P. & Margolin, W. Splitsville: structural and functional insights
498 into the dynamic bacterial Z ring. *Nat Rev Microbiol* **14**, 305-319,
499 doi:10.1038/nrmicro.2016.26 (2016).

500 5 den Blaauwen, T., Hamoen, L. W. & Levin, P. A. The divisome at 25: the road
501 ahead. *Curr Opin Microbiol* **36**, 85-94, doi:10.1016/j.mib.2017.01.007 (2017).

502 6 Erickson, H. P., Anderson, D. E. & Osawa, M. FtsZ in bacterial cytokinesis:
503 cytoskeleton and force generator all in one. *Microbiol Mol Biol Rev* **74**, 504-
504 528, doi:10.1128/MMBR.00021-10 (2010).

505 7 Ortiz, C., Natale, P., Cueto, L. & Vicente, M. The keepers of the ring:
506 regulators of FtsZ assembly. *FEMS microbiology reviews* **40**, 57-67,
507 doi:10.1093/femsre/fuv040 (2016).

508 8 Skoog, K., Söderström, B., Widengren, J., von Heijne, G. & Daley, D. O.
509 Sequential closure of the cytoplasm and then the periplasm during cell
510 division in *Escherichia coli*. *Journal of bacteriology* **194**, 584-586,
511 doi:10.1128/JB.06091-11 (2012).

512 9 Söderström, B. *et al.* Disassembly of the divisome in *Escherichia coli*:
513 evidence that FtsZ dissociates before compartmentalization. *Molecular*
514 *microbiology* **92**, 1-9, doi:10.1111/mmi.12534 (2014).
515 10 Egan, A. J. F. Bacterial outer membrane constriction. *Molecular microbiology*
516 **107**, 676-687, doi:10.1111/mmi.13908 (2018).
517 11 Fu, G. *et al.* In vivo structure of the *E. coli* FtsZ-ring revealed by
518 photoactivated localization microscopy (PALM). *PLoS One* **5**, e12682,
519 doi:10.1371/journal.pone.0012680 (2010).
520 12 Coltharp, C., Buss, J., Plumer, T. M. & Xiao, J. Defining the rate-limiting
521 processes of bacterial cytokinesis. *Proc Natl Acad Sci U S A* **113**, E1044-
522 1053, doi:10.1073/pnas.1514296113 (2016).
523 13 Yang, X. *et al.* GTPase activity-coupled treadmilling of the bacterial tubulin
524 FtsZ organizes septal cell wall synthesis. *Science* **355**, 744-747,
525 doi:10.1126/science.aak9995 (2017).
526 14 Söderström, B., Chan, H., Shilling, P. J., Skoglund, U. & Daley, D. O. Spatial
527 separation of FtsZ and FtsN during cell division. *Molecular microbiology* **107**,
528 387-401, doi:10.1111/mmi.13888 (2018).
529 15 Bisson-Filho, A. W. *et al.* Treadmilling by FtsZ filaments drives peptidoglycan
530 synthesis and bacterial cell division. *Science* **355**, 739-743,
531 doi:10.1126/science.aak9973 (2017).
532 16 Schoenemann, K. M. & Margolin, W. Bacterial Division: FtsZ Treadmills to
533 Build a Beautiful Wall. *Curr Biol* **27**, R301-R303,
534 doi:10.1016/j.cub.2017.03.019 (2017).

535 17 Monteiro, J. M. *et al.* Peptidoglycan synthesis drives an FtsZ-treadmilling-
536 independent step of cytokinesis. *Nature* **554**, 528-532,
537 doi:10.1038/nature25506 (2018).
538 18 Moore, D. A., Whatley, Z. N., Joshi, C. P., Osawa, M. & Erickson, H. P.
539 Probing for Binding Regions of the FtsZ Protein Surface through Site-Directed
540 Insertions: Discovery of Fully Functional FtsZ-Fluorescent Proteins. *Journal of*
541 *bacteriology* **199**, doi:UNSP e00553 10.1128/JB.00553-16 (2017).
542 19 Wu, F., van Schie, B. G., Keymer, J. E. & Dekker, C. Symmetry and scale
543 orient Min protein patterns in shaped bacterial sculptures. *Nat Nanotechnol*
544 **10**, 719-726, doi:10.1038/nnano.2015.126 (2015).
545 20 Hussain, S. *et al.* MreB filaments align along greatest principal membrane
546 curvature to orient cell wall synthesis. *Elife* **7**, doi:10.7554/eLife.32471 (2018).
547 21 Garner, E. C. *et al.* Coupled, circumferential motions of the cell wall synthesis
548 machinery and MreB filaments in *B. subtilis*. *Science* **333**, 222-225,
549 doi:10.1126/science.1203285 (2011).
550 22 Weiss, D. S., Chen, J. C., Ghigo, J. M., Boyd, D. & Beckwith, J. Localization
551 of FtsI (PBP3) to the septal ring requires its membrane anchor, the Z ring,
552 FtsA, FtsQ, and FtsL. *Journal of bacteriology* **181**, 508-520 (1999).
553 23 Söderström, B. *et al.* Coordinated disassembly of the divisome complex in
554 *Escherichia coli*. *Molecular microbiology* **101**, 425-438,
555 doi:10.1111/mmi.13400 (2016).
556 24 Rowlett, V. W. & Margolin, W. 3D-SIM super-resolution of FtsZ and its
557 membrane tethers in *Escherichia coli* cells. *Biophysical journal* **107**, L17-20,
558 doi:10.1016/j.bpj.2014.08.024 (2014).

559 25 Anderson, D. E., Gueiros-Filho, F. J. & Erickson, H. P. Assembly dynamics of
560 FtsZ rings in *Bacillus subtilis* and *Escherichia coli* and effects of FtsZ-
561 regulating proteins. *Journal of bacteriology* **186**, 5775-5781,
562 doi:10.1128/JB.186.17.5775-5781.2004 (2004).
563 26 Young, K. D. The selective value of bacterial shape. *Microbiol Mol Biol Rev*
564 **70**, 660-703, doi:10.1128/MMBR.00001-06 (2006).
565 27 Mannik, J. *et al.* Robustness and accuracy of cell division in *Escherichia coli*
566 in diverse cell shapes. *Proceedings of the National Academy of Sciences of*
567 *the United States of America* **109**, 6957-6962, doi:10.1073/pnas.1120854109
568 (2012).
569 28 Mannik, J., Driessen, R., Galajda, P., Keymer, J. E. & Dekker, C. Bacterial
570 growth and motility in sub-micron constrictions. *Proceedings of the National*
571 *Academy of Sciences of the United States of America* **106**, 14861-14866,
572 doi:10.1073/pnas.0907542106 (2009).
573 29 Zhou, Z. *et al.* The contractile ring coordinates curvature-dependent septum
574 assembly during fission yeast cytokinesis. *Mol Biol Cell* **26**, 78-90,
575 doi:10.1091/mbc.E14-10-1441 (2015).
576 30 Minc, N., Burgess, D. & Chang, F. Influence of cell geometry on division-plane
577 positioning. *Cell* **144**, 414-426, doi:10.1016/j.cell.2011.01.016 (2011).
578 31 Takeuchi, S., DiLuzio, W. R., Weibel, D. B. & Whitesides, G. M. Controlling
579 the shape of filamentous cells of *Escherichia coli*. *Nano Lett* **5**, 1819-1823,
580 doi:10.1021/nl0507360 (2005).
581 32 Wong, F. *et al.* Mechanical strain sensing implicated in cell shape recovery in
582 *Escherichia coli*. *Nat Microbiol* **2**, 17115, doi:10.1038/nmicrobiol.2017.115
583 (2017).

584 33 Monahan, L. G. *et al.* Rapid conversion of *Pseudomonas aeruginosa* to a
585 spherical cell morphotype facilitates tolerance to carbapenems and penicillins
586 but increases susceptibility to antimicrobial peptides. *Antimicrobial agents and*
587 *chemotherapy* **58**, 1956-1962, doi:10.1128/AAC.01901-13 (2014).
588 34 Yao, Q. *et al.* Short FtsZ filaments can drive asymmetric cell envelope
589 constriction at the onset of bacterial cytokinesis. *EMBO J*,
590 doi:10.15252/embj.201696235 (2017).
591 35 Strauss, M. P. *et al.* 3D-SIM Super Resolution Microscopy Reveals a Bead-
592 Like Arrangement for FtsZ and the Division Machinery: Implications for
593 Triggering Cytokinesis. *PLoS biology* **10**, doi:ARTN e1001389
594 10.1371/journal.pbio.1001389 (2012).
595 36 Holden, S. J. *et al.* High throughput 3D super-resolution microscopy reveals
596 *Caulobacter crescentus* in vivo Z-ring organization. *Proceedings of the*
597 *National Academy of Sciences of the United States of America* **111**, 4566-
598 4571, doi:10.1073/pnas.1313368111 (2014).
599 37 Jacq, M. *et al.* Remodeling of the Z-Ring Nanostructure during the
600 *Streptococcus pneumoniae* Cell Cycle Revealed by Photoactivated
601 Localization Microscopy. *mBio* **6**, doi:10.1128/mBio.01108-15 (2015).
602 38 Loose, M. & Mitchison, T. J. The bacterial cell division proteins FtsA and FtsZ
603 self-organize into dynamic cytoskeletal patterns. *Nature cell biology* **16**, 38-46,
604 doi:10.1038/ncb2885 (2014).
605 39 Stricker, J., Maddox, P., Salmon, E. D. & Erickson, H. P. Rapid assembly
606 dynamics of the *Escherichia coli* FtsZ-ring demonstrated by fluorescence
607 recovery after photobleaching. *Proceedings of the National Academy of*

608 *Sciences of the United States of America* **99**, 3171-3175,
609 doi:10.1073/pnas.052595099 (2002).
610 40 Surovtsev, I. V. & Jacobs-Wagner, C. Subcellular Organization: A Critical
611 Feature of Bacterial Cell Replication. *Cell* **172**, 1271-1293,
612 doi:10.1016/j.cell.2018.01.014 (2018).
613 41 Caccamo, P. D. & Brun, Y. V. The Molecular Basis of Noncanonical Bacterial
614 Morphology. *Trends Microbiol* **26**, 191-208, doi:10.1016/j.tim.2017.09.012
615 (2018).
616 42 Gibson, D. G. *et al.* Enzymatic assembly of DNA molecules up to several
617 hundred kilobases. *Nature methods* **6**, 343-U341, doi:10.1038/NMETH.1318
618 (2009).
619 43 Amann, E., Ochs, B. & Abel, K. J. Tightly regulated tac promoter vectors
620 useful for the expression of unfused and fused proteins in *Escherichia coli.*
621 *Gene* **69**, 301-315 (1988).
622 44 Antonov, P. V., Zuiddam, M. R. & Frenken, J. W. M. Fabrication of high-
623 aspect ratio silicon nanopillars for tribological experiments. *J Micro-Nanolith*
624 *Mem* **14**, doi:Artn 044506 10.1117/1.Jmm.14.4.044506 (2015).
625 45 Ayari-Kanoun, A., Aydinoglu, F., Cui, B. & Saffih, F. Silicon nanostructures
626 with very large negatively tapered profile by inductively coupled plasma-RIE. *J*
627 *Vac Sci Technol B* **34**, doi:Artn 06kd01 10.1116/1.4964402 (2016).
628 46 Martin, M. *et al.* Fabrication of high-density Si and SixGe1-x nanowire arrays
629 based on the single step plasma etching process. *J Vac Sci Technol B* **31**,
630 doi:Artn 041806
631 10.1116/1.4812792 (2013).

47 Engstrom, D. S. & Soh, Y. A. Controlling the silicon nanowire tapering angle in dense arrays of silicon nanowires using deep reactive ion etching. *J Vac Sci Technol B* **31**, doi:Artn 021806 10.1116/1.4793500 (2013).

641 **Figures and Tables**

642

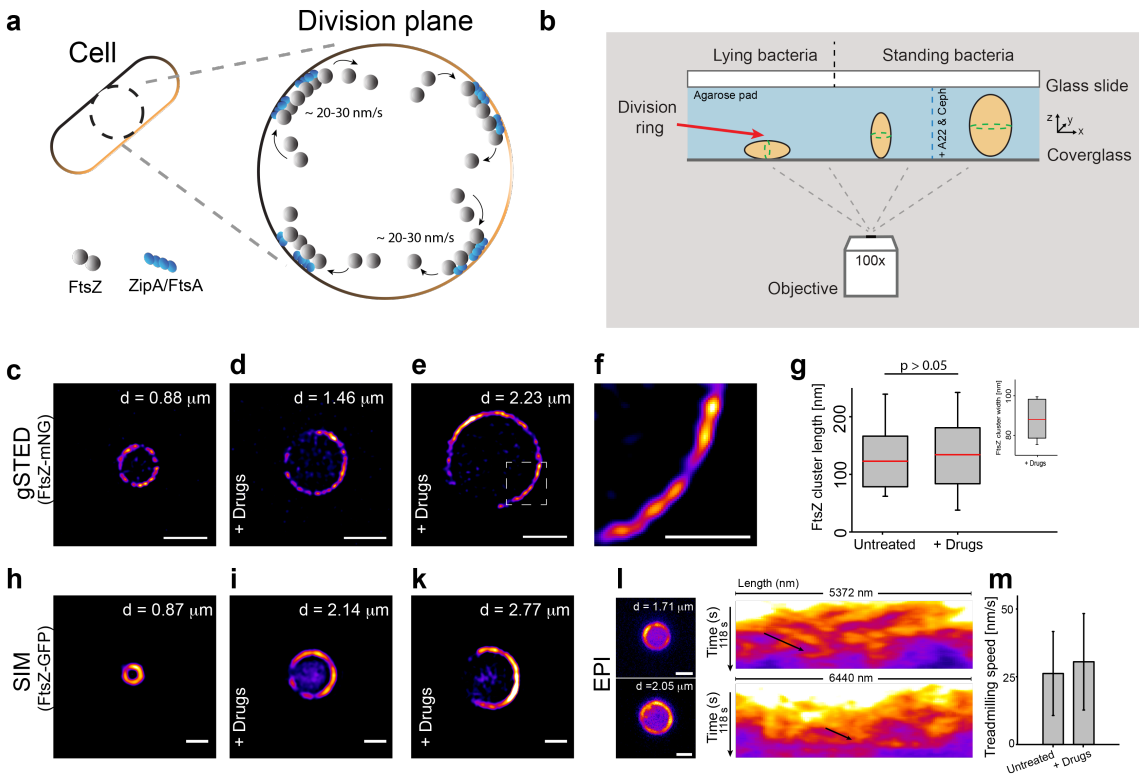

643

644 **Figure 1. Midcell Z-ring assembly is unaffected by increased cell diameter.**

645 **a**, Simplified cartoon showing FtsZ treadmilling at the division plane of an
646 *E. coli* cell. For clarity, only the membrane tethers, FtsA and ZipA, are shown.
647 **b**, Schematic representation of cell placement for imaging. Standing cells were
648 trapped in a vertical position in micron-sized holes in agarose pads created using
649 micron-sized pillars. Conditions for proper division ring placement are met when width
650 < length. The left and middle cells represent untreated cells. The cell on the right has
651 increased dimensions due to drug exposure (A22 and cephalexin). **c**, Time-gated
652 STED (gSTED) image of a typical FtsZ-ring (FtsZ-mNeonGreen) in an untreated
653 standing cell. Scale bar = 1 μm. **d** and **e**, gSTED images of FtsZ-mNeonGreen rings
654 in *E. coli* cells treated with drugs, showing increased ring diameter. Scale bar = 1 μm.
655 "Drugs" refer to A22 and cephalexin. **f**, Close-up of representative FtsZ densities

656 shown in **e**, from a cell with increased diameter. Scale bar = 0.5 μm. **g**, Quantification
657 of FtsZ density lengths in untreated and drug-treated cells. Mean ± S.D. was 122.8 ±
658 43.9 nm (n = 77) and 132.4 ± 48.7 nm (n = 172) for untreated and drug-treated cells,
659 respectively. No statistically significant difference was measured, $p > 0.05$. Inset
660 shows density widths in drug-treated cells, mean ± S.D. = 88.4 ± 9.8 nm (n = 172). **h**
661 **- k**, Structured Illumination Microscopy (SIM) images of FtsZ-GFP in *E. coli* cells (**h**)
662 untreated or (**i** - **k**) treated with drugs. Scale bars = 1 μm. **l**, Snapshots of
663 epifluorescence (EPI) images from time-lapse series of FtsZ-GFP dynamics in drug-
664 treated cells. Scale bars = 1 μm. Corresponding kymographs are shown adjacent to
665 each image. Black arrows point to examples of FtsZ trajectories. **m**, Average
666 treadmilling speed of FtsZ-GFP in untreated (26 ± 15 nm/s, n = 102) and drug-treated
667 cells (30 ± 18 nm/s, n = 102). "d" in (**c** - **e**) and (**h** - **l**) indicates cell diameter.
668
669
670
671
672
673
674
675
676

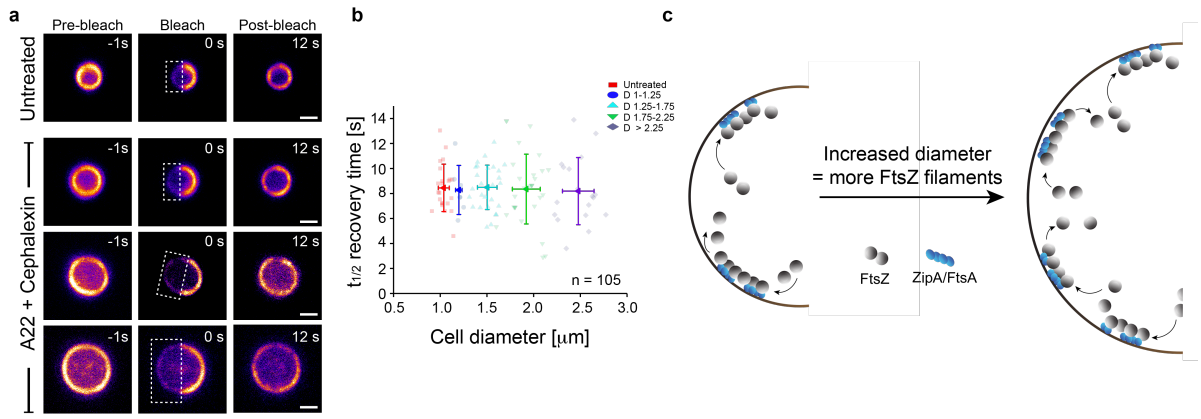

677

678 **Figure 2. Cell size independent recovery of fluorescence in FtsZ-rings.**

679 FRAP measurements on FtsZ-GFP rings in *E. coli* cells trapped standing in a vertical
680 position. **a**, Representative cells of different diameter, untreated or treated with drugs.
681 White boxes indicate bleached areas. Scale bars = 1 μm. **b**, Quantification of FRAP
682 data from untreated cells (red), and drug-treated cells (other colors), showing that
683 fluorescence recovery time is independent of cell diameter (in the range investigated,
684 *i.e.* ~ 1 - 3 μm). n_{tot} = 105. "D" = cell diameter range. (see SI text for detailed values).
685 **c**, Schematic representation of possible FtsZ filament distribution in cells of different
686 diameters. Cells with larger diameter can accommodate a greater number of FtsZ
687 filaments.

688

689

690

691

692

693

694

695

696

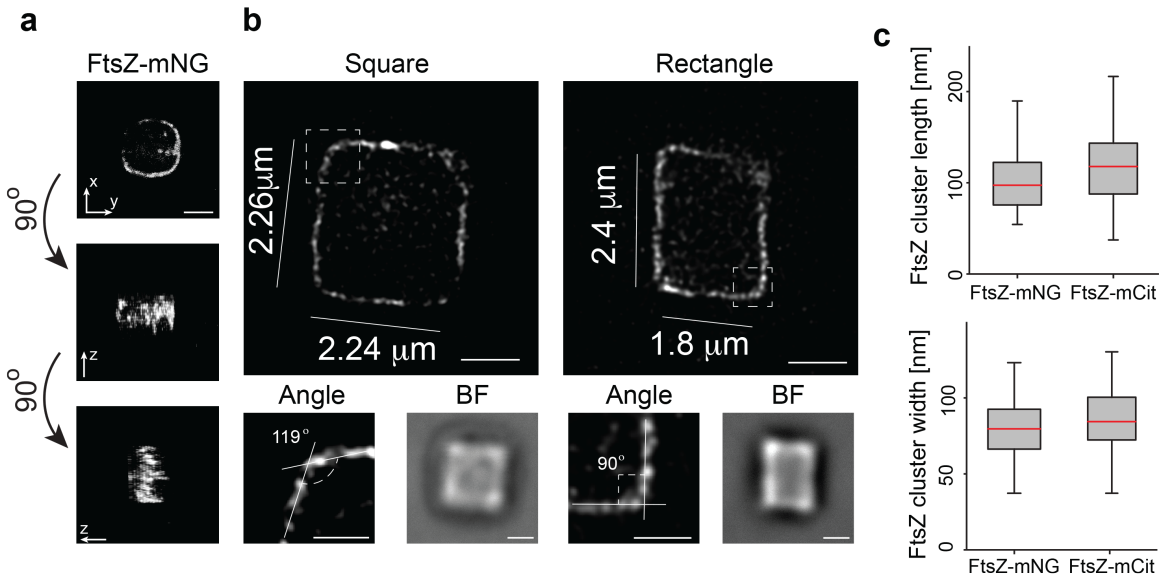

Figure 3. FtsZ-squares and -rectangles in shaped cells.

Drug-treated (A22 and cephalexin) *E. coli* cells expressing FtsZ-mNeonGreen were sculptured into rectangular shapes and imaged using super-resolution STED nanoscopy. **a**, 3D rendering of a confocal Z-stack of an FtsZ-mNeonGreen square, showing only one band of FtsZ. Note that information along the z-axis is elongated. **b**, Representative STED images of FtsZ-mNeonGreen in square (left) and rectangular (right) cells with perimeters ranging from 8.4 to 11.52 µm (compared to WT ~ 3 µm). Additional examples are provided in Supplementary Fig. S9. Close-up images show representative corner angles. BF, brightfield image of corresponding cells. **c**, Quantification of FtsZ cluster dimensions, showing little difference between FtsZ-mNeonGreen (105.4 ± 39.6, 79.6 ± 18.2; length and width, respectively. n = 147) and FtsZ-mCitrine (118.3 ± 41.3, 86.3 ± 22.5; length and width, respectively. n = 162. Example images of FtsZ-mCitrine squares are shown in Supplementary Fig. S10). Scale bars = 1 µm.

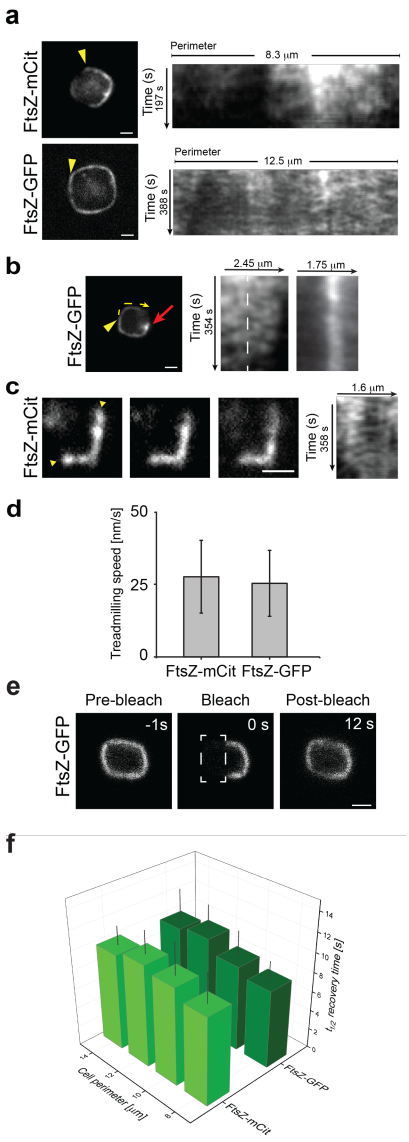

712

713 **Figure 4. FtsZ dynamics in rectangular-shaped cells.**

714 The dynamics of FtsZ in rectangular shapes were assessed by time-lapse imaging
715 and FRAP measurements on *E. coli* cells expressing FtsZ-mCitrine or FtsZ-GFP. **a** -
716 **c**, Snapshot images from time-lapse series of FtsZ-mCitrine or FtsZ-GFP in
717 rectangular shaped cells. Corresponding kymographs are shown next to each image.
718 **a**, Kymographs were taken around the entire perimeter (starting in the upper left
719 corner, moving counter-clockwise, indicated by the yellow arrowheads). **b**,
720 Kymographs were taken along the yellow line starting at the yellow arrowhead (left
721 kymograph), or over the bright spot indicated by the red arrow (right kymograph). The

722 white striped line in **b** indicates the upper left corner of the cell. **c**, Kymograph taken
723 between the yellow arrowheads (top to bottom is left to right in the kymograph). **d**,
724 Average treadmilling speed of FtsZ-mCitrine and FtsZ-GFP in rectangles was 27.6 ±
725 12.5 nm/s (n = 97) and 25.3 ± 11.3 nm/s (n = 122), respectively. **e**, Typical FRAP
726 measurement of FtsZ-GFP in a rectangular *E. coli* cell. Half of the rectangle was
727 bleached. **f**, Average recovery times for FtsZ-mCitrine (light, n_{tot} = 24) and FtsZ-GFP
728 (dark, n_{tot} = 22) in FtsZ-rectangles of various perimeter lengths (see SI text for detailed
729 values). Scale bars = 1 μm.
730
731
732
733
734
735
736
737
738
739
740

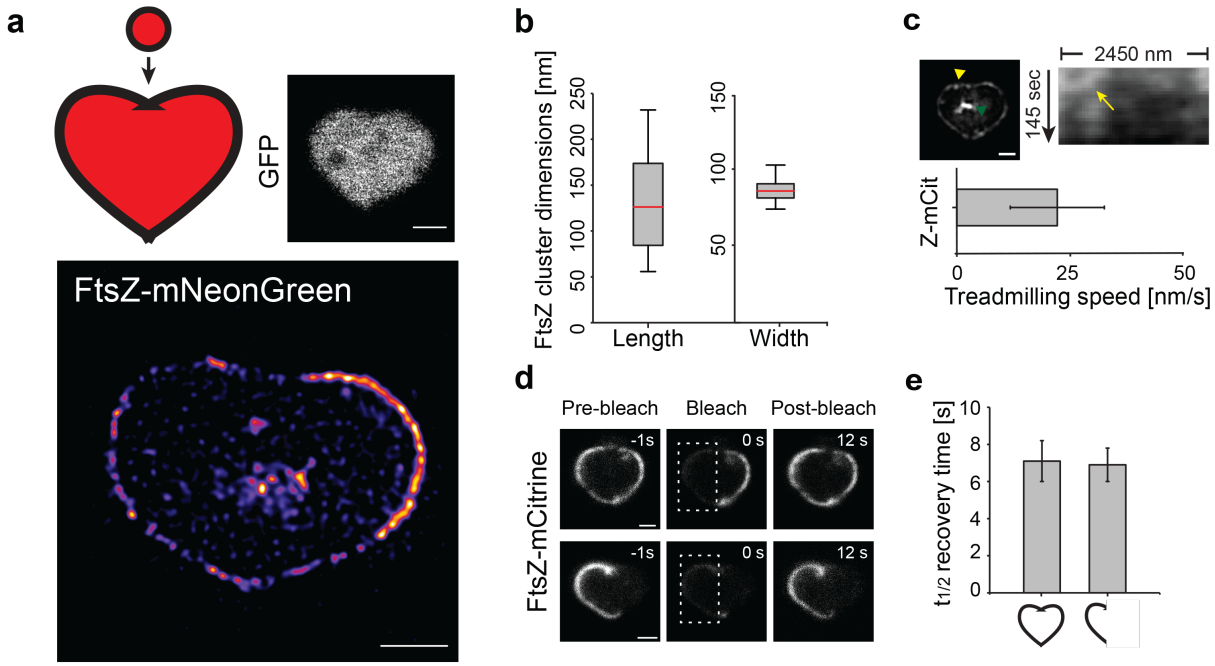

741

742 **Figure 5. FtsZ cluster dimensions and dynamics in heart-shaped cells.**

743 FtsZ behavior in *E. coli* cells sculptured into heart shapes. **a**, Upper left, Cartoon
744 representation of a WT *E. coli* cell and a heart shape, highlighting the large and
745 complex structural changes of a cell-to-heart transition, approximately to scale. Upper
746 right, Drug-treated cell expressing cytoplasmic GFP, shaped as a heart. Lower, STED
747 image of an "FtsZ-heart" (FtsZ-mNeonGreen) in a drug-treated *E. coli* cell. **b**, Lengths
748 and widths of 155 individual FtsZ-mNeonGreen fluorescence densities in cells shaped
749 as hearts. Average length = 129 ± 44 nm and width = 84 ± 9 nm. **c**, Upper row, SIM
750 image from a time-lapse series (epi-fluorescence) of a heart-shaped cell expressing
751 FtsZ-mCitrine. Green arrowhead indicates internal FtsZ clustering. Corresponding
752 kymograph is shown adjacent to the image, and was generated starting at the yellow
753 arrowhead in the SIM image, moving counter-clockwise for the indicated length. The
754 yellow arrow points to an FtsZ trajectory. Lower, average treadmilling speed of FtsZ-
755 mCitrine (Z-mCit) filaments in hearts (22.6 ± 10.4 nm/s, n = 44). **d**, FRAP
756 measurements of FtsZ-mCitrine in heart-shaped cells. Top row, bleaching of half the
757 FtsZ-mCitrine molecules in a 'full' heart. Bottom row, bleaching of a 'half-full' heart. No

difference in recovery time was observed. **e**, Histogram of average $t_{1/2}$ recovery times calculated from FRAP measurements. Recovery in ‘full hearts’: 7.1 ± 1.1 s (n = 24), recovery in ‘half hearts’: 6.9 ± 0.9 s (n = 9).

783

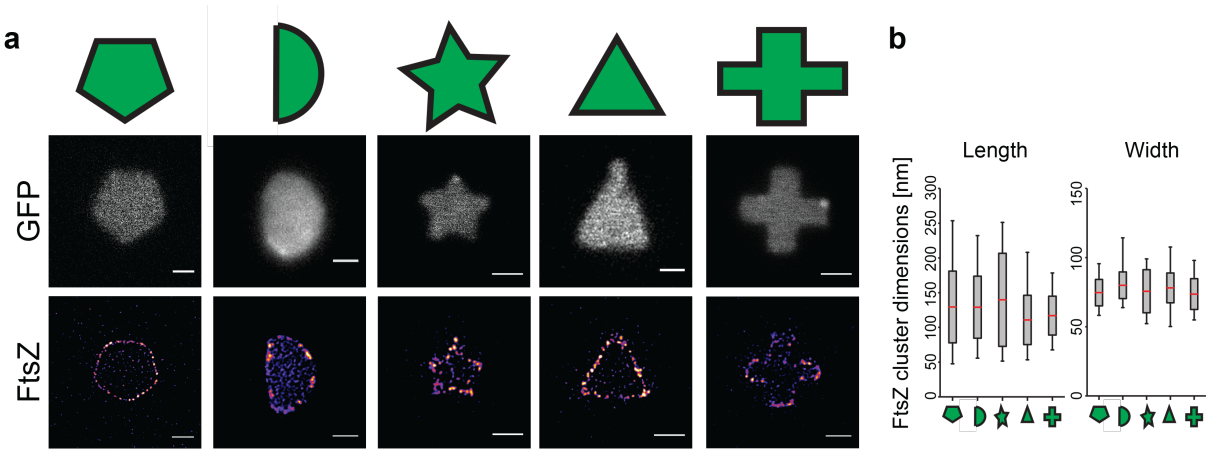

784

785

786 **Figure 6. FtsZ bundle dimensions in complex shapes.**

787 **a**, Cells expressing cytosolic GFP or FtsZ-mCitrine were remodeled into various
788 shapes. Top row, schematic representation of the cell shapes. Middle row,
789 representative cells expressing cytosolic GFP, and sculptured in the corresponding
790 shapes. Bottom row, an FtsZ-pentagon, FtsZ-half-moon, FtsZ-star, FtsZ-triangle and
791 FtsZ-cross in sculptured cells. Scale bars = 1 μm. **b**, Quantification of FtsZ densities
792 by length and width in shaped cells (see SI text for detailed values).

793

FtsZ density dimensions

Cell shape	FP*	Drugs$	Length [nm]	Width [nm]
(WT)	mNG	–	123 ± 44	80 ± 2
	mNG	+	132 ± 48	88 ± 9
	mNG	+	105 ± 40	80 ± 18
	mCit	+	118 ± 41	86 ± 22
	mNG	+	129 ± 44	84 ± 9
	mNG	+	131 ± 52	74 ± 9
	mNG	+	129 ± 45	80 ± 10
	mNG	+	140 ± 67	76 ± 16
	mNG	+	110 ± 35	78 ± 11
	mNG	+	119 ± 21	71 ± 18

* Fluorescent protein; mNG = mNeonGreen, mCit = mCitrine
$ Drugs; A22 [16 μM] and Cephalexin [20 μM]

794
795

796 **Table 1. Summary of FtsZ density dimensions at midcell in various cell**

797 **shapes.** In all cell shapes, the average measured density lengths were within 17 %

798 of WT, while average widths were within 13 %. Numbers represent mean ± S.D.

799 Note that values are rounded to whole integers.

800

801

802

803

804

FtsZ Dynamics

Cell shape	FP*	Drugs$	Treadmilling speed [nm/s]	$t_{1/2}$ recovery [s]
(WT)	GFP	–	26 ± 15	8 ± 2
	GFP	+	30 ± 18	8 ± 2
	mCit	+	28 ± 13	10 ± 3
	GFP	+	25 ± 11	9 ± 3
	mCit	+	23 ± 10	7 ± 1

805 * Fluorescent protein; mCit = mCitrine $Drugs; A22 [16 μM] and Cephalexin [20 μM]

806

807 **Table 2. Summary of FtsZ dynamics in various cell shapes.**

808 Numbers represent mean ± S.D. Note that values are rounded to whole integers.

809